

Assessing the Impact of Defects on Lead-Free Perovskite-Inspired Photovoltaics via Photoinduced Current Transient Spectroscopy

Vincenzo Pecunia,* Jing Zhao, Chaewon Kim, Blair R. Tuttle, Jianjun Mei, Fengzhu Li, Yueheng Peng, Tahmida N. Huq, Robert L. Z. Hoyer, Nicola D. Kelly, Siân E. Dutton, Kai Xia, Judith L. MacManus-Driscoll, and Henning Sirringhaus


The formidable rise of lead-halide perovskite photovoltaics has energized the search for lead-free perovskite-inspired materials (PIMs) with related optoelectronic properties but free from toxicity limitations. The photovoltaic performance of PIMs closely depends on their defect tolerance. However, a comprehensive experimental characterization of their defect-level parameters—concentration, energy depth, and capture cross-section—has not been pursued to date, hindering the rational development of defect-tolerant PIMs. While mainstream, capacitance-based techniques for defect-level characterization have sparked controversy in lead-halide perovskite research, their use on PIMs is also problematic due to their typical near-intrinsic character. This study demonstrates on four representative PIMs ($\text{Cs}_3\text{Sb}_2\text{I}_9$, $\text{Rb}_3\text{Sb}_2\text{I}_9$, BiOI , and AgBiI_4) for which Photoinduced Current Transient Spectroscopy (PICTS) offers a facile, widely applicable route to the defect-level characterization of PIMs embedded within solar cells. Going beyond the ambiguities of the current discussion of defect tolerance, a methodology is also presented to quantitatively assess the defect tolerance of PIMs in photovoltaics based on their experimental defect-level parameters. Finally, PICTS applied to PIM photovoltaics is revealed to be ultimately sensitive to defect-level concentrations <1 ppb. Therefore, this study provides a versatile platform for the defect-level characterization of PIMs and related absorbers, which can catalyze the development of green, high-performance photovoltaics.

1. Introduction

Over the past decade, lead-halide perovskites have risen to prominence in photovoltaics—their certified single-junction power conversion efficiencies (PCEs) now above 25%—as well as in other optoelectronic applications such as light-emitting devices, photodetectors, and transistors.^[1–6] A key enabler of this formidable rise is their defect tolerance.^[7–9] Indeed, while compositional and structural defects are inevitably present in polycrystalline semiconductors deposited at low temperatures, through solution-based methods,^[10] and in common laboratory settings, thin-film lead-iodide-based perovskites remarkably manifest an optoelectronic behavior that is largely insensitive to such defects.^[9,11–15] Researchers have thus set out to identify safer and stable alternatives to lead-iodide-based perovskites that could replicate their defect tolerance.^[16–18] This has resulted in the exploration of lead-free perovskite-inspired materials (PIMs) that can be processed using facile, low-temperature methods and that possess electronic

Prof. V. Pecunia, J. Zhao, Dr. C. Kim, J. Mei, F. Li, Y. Peng, K. Xia
Institute of Functional Nano & Soft Materials (FUNSOM)
Jiangsu Key Laboratory for Carbon-Based Functional Materials & Devices
Soochow University
199 Ren'ai Road, Suzhou, Jiangsu 215123, P. R. China
E-mail: vp293@suda.edu.cn

Prof. B. R. Tuttle
Department of Physics
Penn State Behrend
Erie, PA 16563, USA

 The ORCID identification number(s) for the author(s) of this article can be found under <https://doi.org/10.1002/aenm.202003968>.

© 2021 The Authors. Advanced Energy Materials published by Wiley-VCH GmbH. This is an open access article under the terms of the Creative Commons Attribution License, which permits use, distribution and reproduction in any medium, provided the original work is properly cited.

DOI: 10.1002/aenm.202003968

T. N. Huq, Prof. J. L. MacManus-Driscoll
Department of Materials Science and Metallurgy
University of Cambridge
27 Charles Babbage Road, Cambridge CB3 0FS, UK

Dr. R. L. Z. Hoyer
Department of Materials
Imperial College London
Exhibition Road, London SW7 2AZ, UK

N. D. Kelly, Prof. S. E. Dutton, Prof. H. Sirringhaus
Cavendish Laboratory
University of Cambridge
J J Thomson Avenue, Cambridge CB3 0HE, UK

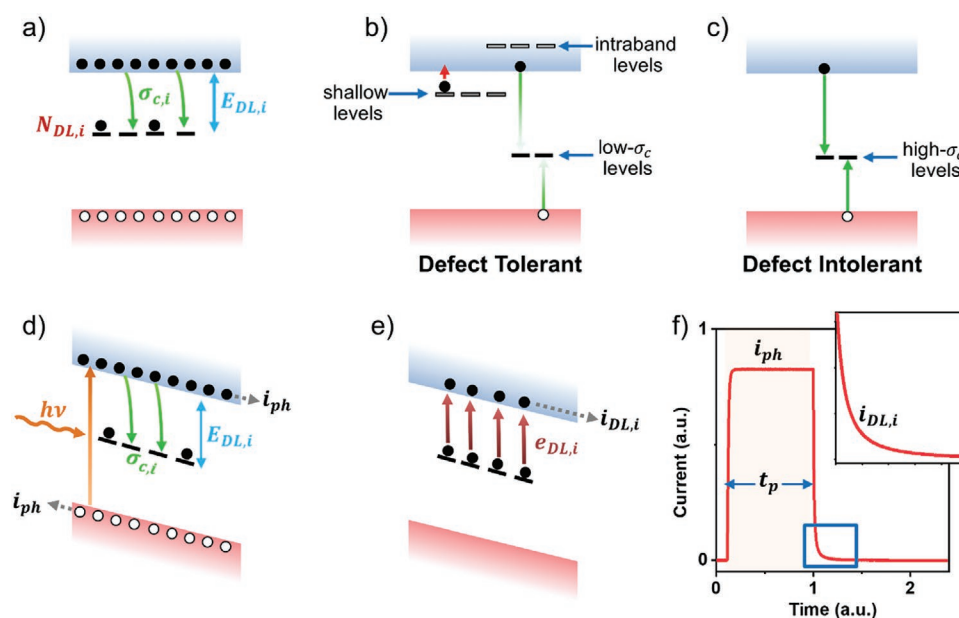


Figure 1. a) Charge carrier capture by a defect level and the associated defect parameters ($\sigma_{c,i}$: capture cross section; $N_{DL,i}$: concentration; $E_{DL,i}$: energy depth). For the sake of simplicity, only electron capture is shown. b) Defect tolerant semiconductor and c) defect intolerant semiconductor (red arrow: emission from a defect level; faded green arrows: low-probability carrier capture; solid green arrows: high-probability carrier capture). For the sake of simplicity, only intraband and shallow levels associated/interacting with the conduction band are shown in (b). d) Defect-level filling during illumination in a PICTS experiment (i_{ph} : photocurrent). Only electron capture is shown for the sake of simplicity. e) Defect-level emptying after the termination of a light pulse in a PICTS experiment ($i_{DL,i}$: defect-level emptying current; $e_{DL,i}$: emission rate). f) Schematic of the current waveform in a PICTS experiment, where t_p is the duration of the light pulse (inset: a magnified version of the deep-level-emptying current, which corresponds to the region within the blue rectangle).

properties similar to lead-halide perovskites, while being unencumbered by the same toxicity concerns.^[19–21] In addition to solar photovoltaics, PIMs have considerable potential for indoor photovoltaics (IPVs), building-integrated photovoltaics, tandem photovoltaics, photocathodes for water splitting, photodetectors, light-emitting devices, and radiation detectors.^[21–31]

In view of the key role that defect tolerance has played in determining the success of lead-halide perovskites, identifying how defect tolerance arises and how it can be designed into a material has been a key driving force for PIM development.^[7,8,23,32–34] While the concept of defect tolerance has not been rigorously and quantitatively defined, with different interpretations being proposed,^[8,23,32,35,36] an absorber is generally regarded as defect tolerant if its compositional and structural defects result in electronic states (so-called defect levels) that are either “shallow,” or with small capture cross-sections, or that fall within the energy bands (Figure 1a,b).^[7,9,12,15,32,35] Indeed, a shallow defect level (see below) would easily re-emit a captured carrier to the nearest energy band due to thermal excitation (Figure 1b). Consequently, it would act as a *trap* and not as a *recombination center* (i.e., the probability of carrier re-emission would be orders of magnitude larger than that of capturing a carrier of the opposite polarity, which would lead to carrier recombination), the latter case being highly detrimental to photovoltaic performance. Additionally, as the capture cross-section quantifies the ease with which a defect level captures a mobile carrier (Figure 1a), a small value of this parameter would contribute to limiting the “activity” of the corresponding defect level. This is schematically depicted in Figure 1b, which

represents the case of a defect tolerant semiconductor. By contrast, if a semiconductor has “deep” defect levels with large capture cross-sections (Figure 1c), then its mobile carriers would be easily captured by such defect levels and would eventually recombine nonradiatively—i.e., the semiconductor would not be tolerant to such defects.

It is important to note that the classification of a defect level as shallow or deep (i.e., as a trap instead of a recombination center) does not simply depend on how its energy depth $E_{DL,i}$ (Figure 1a) compares to the thermal energy $k_B T$ (where k_B is the Boltzmann constant and T is the absolute temperature).^[37–39] Indeed, such a distinction is determined by the position of the demarcation energies associated with the defect level, which depends not only on $E_{DL,i}/k_B T$ but also on the capture cross-section of the defect level (in addition to the overall defect level landscape within the bandgap of the semiconductor, the carrier effective masses, and the generation rate in the semiconductor).^[37–39] Therefore, it is apparent that the energy depths and capture cross-sections of the defect levels in a PIM are key determinants of its defect tolerance.

From a compositional point of view, the defect tolerance of PIMs has been linked to the presence of a large, highly polarizable metal cation with an ns^2 electronic configuration and in a stable oxidation state.^[19,32] This has motivated a rapidly growing interest in PIMs based on antimony and bismuth, which meet these requirements.^[19,20] Despite the comparatively small scale and short time span of the ensuing research endeavor, appreciable progress in bismuth- and antimony-based PIM photovoltaics has been achieved. For instance, the reported single-junction

PCE is up to 5.6% for silver bismuth sulfoiodides under AM 1.5G illumination,^[40] while the IPV efficiencies are up to $\approx 5\%$ for $\text{Cs}_3\text{Sb}_2\text{Cl}_x\text{I}_{9-x}$ and BiOI (i.e., already within the same range of IPV industry-standard hydrogenated amorphous silicon).^[25]

Given the essential role that defects play in determining the photovoltaic performance and potential of PIMs, a quantitative experimental characterization of their defect properties would be highly beneficial to the field as a whole because: it would contribute to the identification of the most promising PIMs without extensive device optimization; it would allow the rational identification of the relationship between defect tolerance and structure/composition; it would catalyze the development of defect-healing strategies; and it would provide a much needed experimental support to computational studies, thereby potentially aiding the discovery of new defect-tolerant absorbers. Specifically, such a characterization should allow the determination of the so-called defect-level parameters (or defect parameters, in short)—i.e., volumetric concentration, energy depth, and capture cross-section—for each of the defect levels present. Importantly, to the best of our knowledge, an experimental and quantitative assessment of the defect parameters of PIMs has not been pursued to date. Indeed, the experimental characterization of the defect levels in PIMs has thus far been largely phenomenological. It has typically relied on space-charge-limited-current (SCLC) measurements and photoluminescence lifetimes extracted from time-resolved photoluminescence (TPRL) experiments.^[41–44] These techniques, however, do not distinguish among the different defects present in a PIM, nor they allow the assessment of their defect parameters.

Deep-level transient spectroscopy (DLTS) and thermal admittance spectroscopy (TAS) are widely regarded as the gold-standard techniques for the experimental characterization of the defect parameters of a semiconductor.^[45] Specifically, DLTS and TAS rely on the application of a time-varying voltage to enable the filling and emptying of the defect levels.^[45] These techniques are widely applied to doped semiconducting layers, given that in a doped semiconductor the charges needed for defect-level filling are supplied directly from the semiconductor bulk in the immediate vicinity of the edge of a depletion region.^[45] However, capacitance-based techniques are particularly problematic in high-resistivity materials, which may have low carrier density (hence a long dielectric relaxation time) as well as low carrier mobility (hence a long transit time).^[46–49] Specifically, capacitance-based defect-level spectroscopies in near-intrinsic semiconductors—as typically the case for PIMs^[26,43,44,50–65] (Note S1, Supporting Information)—are limited by the fact that the charges required for defect-level filling are not readily available in the semiconductor and need to be transported over a finite distance (e.g., from the electrodes).^[47–49] Additionally, the applicability of DLTS and TAS to perovskites has been recently brought into question.^[66,67] Indeed, it has been recognized that these capacitance-based techniques involve complex processes in perovskite devices (including processes in the charge transport layers adjacent to the perovskite layer), which hamper or preclude the straightforward use of these techniques for the characterization of defect levels in perovskites.^[66–68] Awni et al. found that this is compounded by the insulating nature of the perovskite layers.^[66] In light of these limitations, it is therefore not surprising that a comprehensive experimental assessment of the defect parameters of lead-free PIMs has not been pursued to date.

To the end of contributing quantitative, experimental insight into the defect properties of PIMs, herein we go beyond the above mainstream approaches and explore the applicability of Photoinduced Current Transient Spectroscopy (PICTS) for the straightforward assessment of the defect parameters of PIMs. We demonstrate its wide applicability to lead-free PIMs by conducting a PICTS investigation of four representative absorbers, including $\text{A}_3\text{Sb}_2\text{I}_9$ compounds (with A^+ being a monovalent cation), BiOI, and an Ag-Bi-I ruddorffite. Elaborating on the resultant findings, we then present a versatile methodology that builds on the PICTS-determined defect parameters to deliver a quantitative assessment of the defect tolerance of PIMs in the photovoltaic context, thus delivering insight beyond the qualitative arguments put forward to date. Finally, we quantitatively discuss the defect-level detection capability of PICTS applied to PIM solar cells, thereby providing a concrete assessment of the future potential of this technique to become a standard tool for the defect-level characterization of materials of this class and related absorbers (e.g., perovskites). This study thus brings to the fore a widely applicable experimental approach for the quantitative assessment of the impact of defects on PIM photovoltaics, which could realistically catalyze the identification of easy-to-make green absorbers for environmentally friendly, high-performance photovoltaics.

2. Results and Discussion

2.1. Photoinduced Current Transients as a Probe into the Defect Levels of PIMs

The application of mainstream capacitance-based spectroscopies (e.g., DLTS and TAS) to PIM solar cells would be problematic^[47–49,66] and may not allow the determination of their defect parameters^[66] due to the near-intrinsic character typical of PIMs^[26,43,44,50–65] (Note S1 and Table S1, Supporting Information). This pointed us to the need to pursue alternative current-based spectroscopic approaches. While current-based DLTS (I-DLTS) could potentially provide a solution, in fact, I-DLTS involves the pulsing of a voltage across the semiconductor of interest.^[45] Consequently, owing to the polarization behavior and the mixed electronic-ionic conductivity that may occur in PIMs, I-DLTS would be prone to spurious effects that could mask the defect-related dynamics.^[67–70] Furthermore, considering that I-DLTS relies on carrier injection at the electrode/semiconductor interface for defect-level filling,^[45] we reasoned that I-DLTS would lead to nonuniform defect-level filling in association with the semiconducting layers commonly used in PIM photovoltaics, which are polycrystalline and present stoichiometric nonuniformities. Indeed, in such a case, defect-level filling may be localized to the surroundings of high-conductance pathways,^[71,72] thereby preventing the straightforward and reliable extraction of the defect parameters. Therefore, we envisioned that the ideal spectroscopy for the in situ characterization of the defect levels in a PIM embedded within a solar cell should meet the two following criteria: it should rely on *volume* injection of carriers for defect-level filling in order to probe bulk defect levels; and it should allow the PIM device to remain at a fixed terminal voltage in order to prevent sizeable polarization effects.

In light of the above, we pursued an experimental strategy for the characterization of defect levels in PIMs that involves the monitoring of the current transients in PIM solar-cell device stacks under pulsed illumination and with a fixed voltage across (e.g., 0 V). This strategy comprises the sequence of steps illustrated in Figure 1d–f. First, the PIM device is illuminated through its transparent input electrode with a near-monochromatic light pulse of duration t_p and photon energy $h\nu > E_g$ (Figure 1d), where E_g is the PIM's bandgap. In the presence of volume photo-generation, the defect levels present in the PIM would capture some of the photocarriers (Figure 1d). For a sufficiently long t_p , a steady state would be reached under illumination, with a constant photocurrent traversing the device stack and a constant density of charge carriers populating the defect levels (Figure 1d,f). Once the light pulse ends, mobile carriers would quickly recombine or drift out of the device, leading to a rapid drop in the overall current (Figure 1f). However, carriers populating the defect levels would be thermally re-emitted into the respective bands at a much slower rate—as determined by their emission kinetics—thereby resulting in a long-lived current tail (Figure 1e,f). Therefore, the current flowing through the device after the light pulse terminates would provide a window into the defect-level emptying kinetics, potentially allowing the determination of the defect parameters.

The strategy we have just outlined in fact constitutes the foundation of a specialized defect-level spectroscopy technique

named PICTS, which was developed in the early days of GaAs research as a viable alternative to DLTS for the study of defect levels in semi-insulating semiconductors.^[46,73] To the best of our knowledge, no report has appeared to date examining the general applicability of PICTS to lead-free PIMs, nor has PICTS been adopted in lead-halide perovskite research.^[74,75]

2.2. Defect-Level Characterization of Representative PIMs

To explore the general viability of studying the defect properties of lead-free perovskite-inspired semiconductors via PICTS, we investigated its application to four representative PIMs that have recently attracted a considerable amount of attention in photovoltaics research. First, we considered two antimony-based absorbers (see structures in Figure 2a): 0D $\text{Cs}_3\text{Sb}_2\text{I}_9$, which features isolated $[\text{Sb}_2\text{I}_9]^{3-}$ bi-octahedra,^[50,60] and 2D $\text{Rb}_3\text{Sb}_2\text{I}_9$, which has a layered structure based on sheets of staggered, corner-sharing $[\text{SbI}_6]^{3-}$ octahedra.^[61,62] These compounds are representative of the wider class of 0D and 2D absorbers with a general formula $\text{A}_3\text{B}_2\text{X}_9$, where A^+ is a monovalent cation, $\text{B}^{3+} = \text{Sb}^{3+}$ or Bi^{3+} , and X^- is a halide anion.^[21] Additionally, we investigated two bismuth-based PIMs (see structures in Figure 2a): BiOI , a V-VI-VII material with a layered structure composed of layers of I-Bi-O-Bi-I held together with van

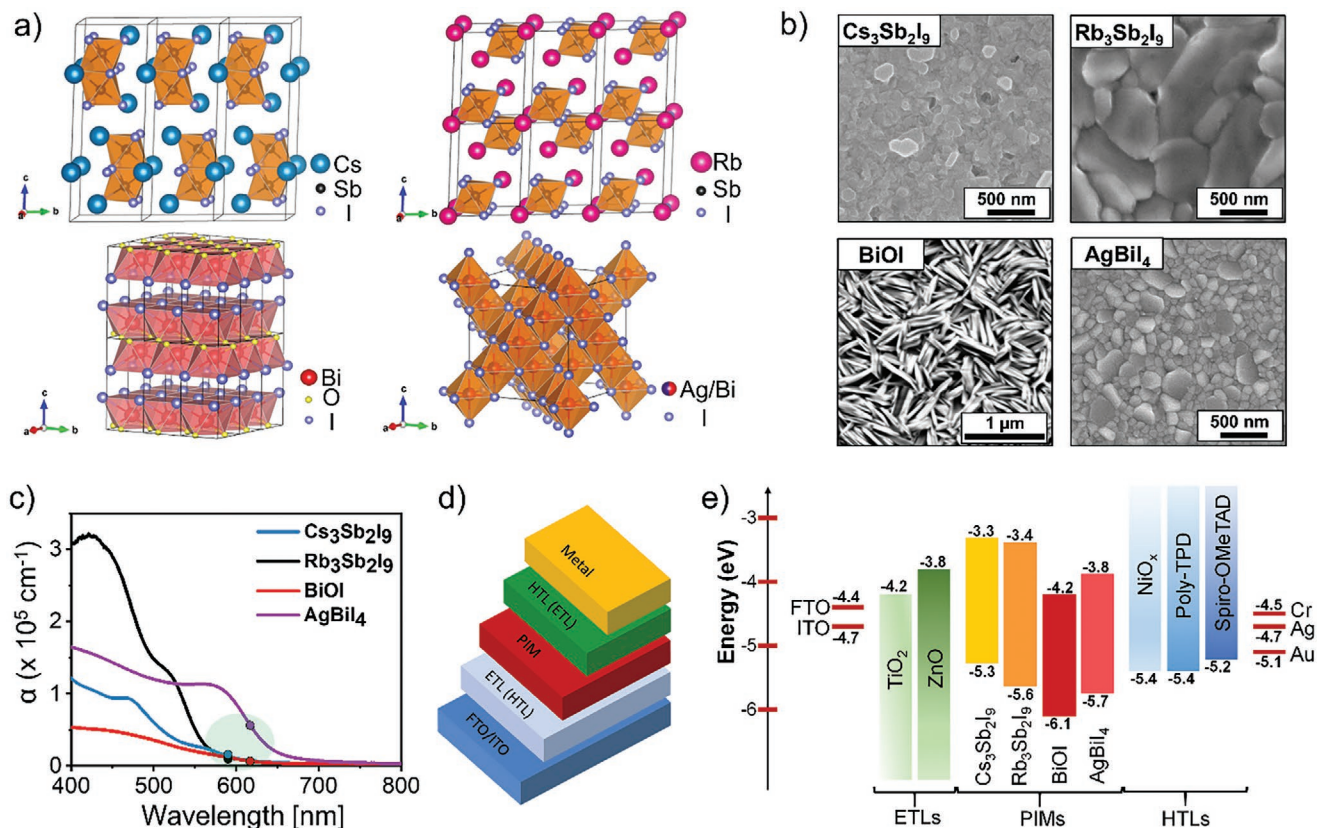


Figure 2. a) Crystal structures, b) top-down SEM images, and c) absorption coefficients of $\text{Cs}_3\text{Sb}_2\text{I}_9$, $\text{Rb}_3\text{Sb}_2\text{I}_9$, BiOI , and AgBiI_4 . The absorption coefficient of BiOI was obtained from ref. [59]. The circles overlaid on the absorption coefficient traces correspond to the dominant wavelength of the light-emitting diodes (LEDs) used as sources in the PICTS experiments. d) Schematic of the device stack. e) Energy levels of the electrode materials, electron-transport materials (ETLs), PIMs, and hole-transport materials (HTLs) used in the PIM devices.^[26,51,60,62,80]

der Waals interactions;^[59,76] and AgBiI_4 , a representative of the ruddorffite family with a general formula $\text{Ag}_a\text{Bi}_b\text{I}_x$ ($x = a + 3b$), which features a three-dimensional lattice of edge-sharing $[\text{BiI}_6]^{3-}$ or $[\text{AgI}_6]^{5-}$ octahedra.^[77,78]

We deposited the representative PIMs via solution-based methods (in the case of $\text{Cs}_3\text{Sb}_2\text{I}_9$, $\text{Rb}_3\text{Sb}_2\text{I}_9$, and AgBiI_4) or thermal chemical vapor deposition (in the case of BiOI) (details in the Experimental Section and Note S2, Supporting Information). Thin films obtained in all cases had a compact morphology, as observed via Scanning Electron Microscopy (SEM) (Figure 2b). Their X-ray diffraction (XRD) patterns (Figure S1, Supporting Information) and absorption coefficients (Figure 2c) were consistent with the literature.^[59,60,62,78] Further, these films manifested a near-intrinsic character, as we already demonstrated for $\text{Cs}_3\text{Sb}_2\text{I}_9$, $\text{Rb}_3\text{Sb}_2\text{I}_9$, and BiOI in our prior publications^[59,60,62] (see also Note S1 and Table S1, Supporting Information) and as we determined for AgBiI_4 via Ultraviolet Photoelectron Spectroscopy (UPS) in the present study (Table S1 and Figure S2, Supporting Information). We embedded such thin films into sandwich-type device stacks (Figure 2d) comprising electrodes and charge transport layers (Figure 2e) commonly employed in the relevant photovoltaic literature.^[59,60,62,79] This was with a view to assessing the viability of PICTS for the in situ characterization of the defect levels in PIM layers grown and processed within complete solar cell device stacks, which could ultimately provide insight into the impact of the defect levels on the PIMs' photovoltaic behavior.

The four types of PIM devices were illuminated with rectangular light pulses of irradiance in the range of $50\text{--}500\ \mu\text{W cm}^{-2}$ and duration t_p equal to $1\text{--}1.5\ \text{s}$ (details in the Experimental Section). The light sources employed were light-emitting diodes (LEDs) narrowly emitting around a wavelength λ_{LED} equal to 590 or $617\ \text{nm}$ (details in the Experimental Section). The wavelength λ_{LED} was selected in order to ensure above-bandgap illumination as well as volume photogeneration (i.e., $\alpha(\lambda_{\text{LED}})L \approx 1$, where α and L are the PIM's absorption coefficient and thickness, respectively) in each of the PIMs.

Representative current transients acquired from the PIM devices in response to the above-bandgap rectangular light pulses are shown in Figure 3. For all materials, the selected duration of the light pulses was sufficient for the photocurrent to reach a level within 2% of the asymptotic steady-state value under illumination (Figure 3). The rising edge of the transients after light turn-on reflects the convolution of charge transport, generation, recombination, and trapping effects.^[81–83] Specifically, the photocurrent traces from $\text{Cs}_3\text{Sb}_2\text{I}_9$, BiOI , and AgBiI_4 devices right after light turn-on exhibited a similar time evolution as the falling edges after light turn-off. Therefore, the shape of the rising edges in such transients can be traced to trapping effects, as the photocurrent can reach the steady state only after trap-filling is complete.^[81–83] As to the $\text{Rb}_3\text{Sb}_2\text{I}_9$ devices, their transients manifested an overshoot right after light turn-on, which is consistent with an overall recombination time that is initially higher than the carrier transit time yet gradually decreases as more carriers become trapped.^[81–83]

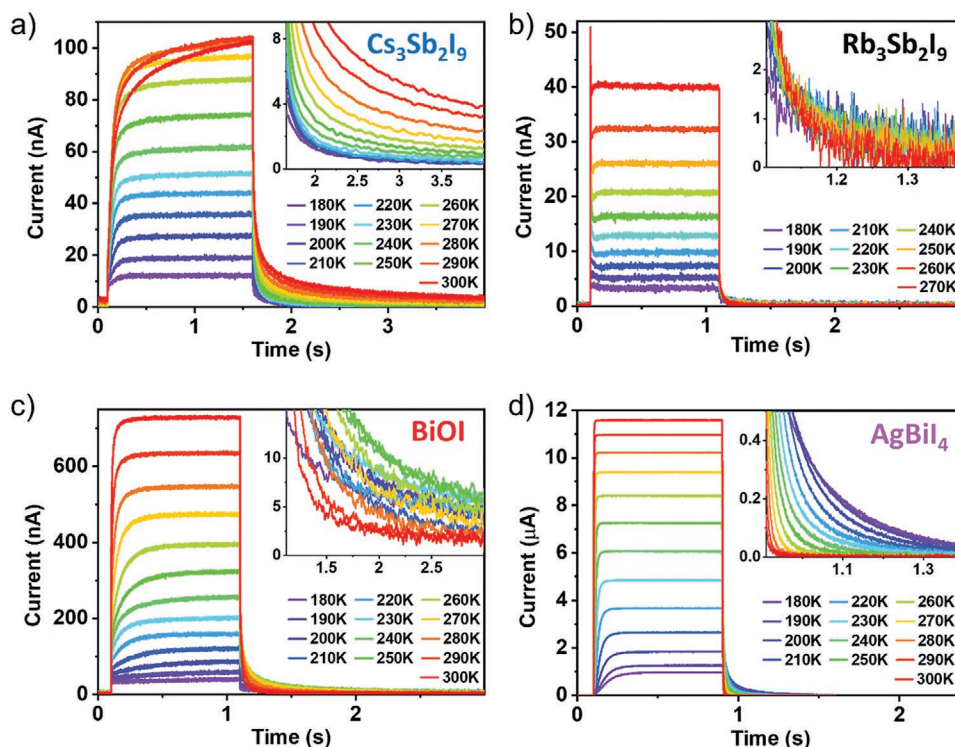


Figure 3. Representative variable-temperature current transients recorded from PICTS experiments on a) $\text{Cs}_3\text{Sb}_2\text{I}_9$ devices, b) $\text{Rb}_3\text{Sb}_2\text{I}_9$ devices, c) BiOI devices, and d) AgBiI_4 devices (insets: magnified view of the current tails ensuing the termination of the light pulses). While the transients presented here are separated by a temperature step of $10\ \text{K}$ for the sake of clarity, in fact, the defect-level analysis presented in this study relies on considerably larger datasets comprising transients acquired with a temperature step of $1\ \text{K}$.

After light turn-off, the current first underwent a rapid drop to a fraction of the steady-state photocurrent value (Figure 3), and subsequently exhibited a long-lived tail (insets of the plots in Figure 3). The initial rapid drop can be attributed to recombination and drift (Note S3, Supporting Information), which jointly lead to the removal of mobile photocarriers from the PIM layer. By contrast, in view of its much slower rate, the ensuing long-lived current tails can be traced to carriers that are slowly released from the defect levels in the PIM layer, consistent with the PICTS framework outlined in Section 2.1.

Under assumptions that commonly hold in PIM solar cells, we derived (Note S4, Supporting Information) that the current arising from carrier emission from a mono-energetic defect level in a PIM would amount to

$$i_{\text{DL},i}(t) = q \frac{1}{1 + \frac{\mu\tau|E|}{L}} V N_{\text{DL},i} e_{\text{DL},i} \exp(-e_{\text{DL},i}t) \quad (1)$$

Here, $N_{\text{DL},i}$ is the volumetric concentration of the defect level and $e_{\text{DL},i}$ is its emission rate. Additionally, q is the elementary charge, μ is the carrier mobility in the relevant band, τ is the lifetime of the emitted carrier, E is the electric field, and L and V are the PIM layer thickness and volume, respectively. Equation (1) captures both the defect-level emptying kinetics (via $e_{\text{DL},i}$) as well as the impact of carrier transport and recombination (through the drift length $\mu\tau E$). We note that we derived Equation (1) to specifically model the defect-level emptying in rectifying sandwich-type devices—such as PIM solar cells—considering that the model widely reported in the PICTS literature is not applicable here because it only covers the rather distinct case of planar photoconductive devices.^[46,84] Inspection of Equation (1) reveals that the current associated with defect-level emptying in a PIM solar cell has the form

$$i_{\text{DL},i}(t) = K e_{\text{DL},i} \exp(-e_{\text{DL},i}t) \quad (2)$$

where K is a prefactor that aggregates materials and device parameters. Equation (2) shows that the decay rate of the current is determined by the emission rate $e_{\text{DL},i}$ of the defect level, which, according to the principle of detailed balanced, can be written as

$$e_{\text{DL},i} = \sigma_{\text{c},i} v_{\text{th}} N_{\text{eff}} \exp(-E_{\text{DL},i}/k_{\text{B}}T) \quad (3)$$

where $\sigma_{\text{c},i}$ is the capture cross section of the defect level, $E_{\text{DL},i}$ is the energy depth of the defect level with respect to the relevant energy band, k_{B} is the Boltzmann constant, T is the absolute temperature, and v_{th} and N_{eff} are the carrier thermal velocity and the effective density of states, respectively, in the relevant energy band.^[45]

In view of the thermally activated behavior of carrier emission from a defect level (Equation 3), current transients from PIM devices under pulsed illumination were acquired within the temperature range 180–300 K (Figure 3) in order to determine the energy depths $E_{\text{DL},i}$ and the capture cross-sections $\sigma_{\text{c},i}$ of their defect levels. Importantly, all of the PIMs considered herein did not exhibit phase transitions (Figure S1 and Note S5, Supporting Information) and manifested stable photocurrent

responses (Note S6 and Figure S3, Supporting Information) in the relevant temperature ranges. Such structural and optoelectronic stability is essential for Equations (1)–(3) to be applicable for the characterization of the defect levels present in PIMs at room temperature—i.e., the defect levels relevant to their solar cell operation.

Given that a PIM may contain multiple defect levels with rather distinct emission rates, the long-lived current ensuing the termination of the light pulses (Figure 3) may arise from the superposition of different contributions of the type given by Equations (1) and (2). Additionally, it is necessary to take into account that the deep-level-emptying current transients branch off from the initial steep current decays (associated with drift/recombination; see Note S3, Supporting Information) following light termination, whose magnitude is affected by the varying levels of steady-state photocurrent (Figure 3). Further, the deep-level-emptying current transients are superimposed on dark current components, which may appreciably vary with temperature (e.g., see Figure 3a vs Figure 3d). While this precludes the analysis of the recorded current transients in Figure 3 by direct visual inspection, it is possible to reliably extract the defect-level-emptying kinetics by computing the corresponding PICTS spectra shown in Figure 4a, which inherently detect the current components of the type given by Equations (1) and (2) (Note S7, Supporting Information).^[46,84] This is analogous to the procedure developed by D. V. Lang for DLTS data analysis.^[45,85] In particular, due to its greater reliability, we adopted the integral four-gate approach (Note S7, Supporting Information) to derive the PICTS spectra for $\text{Cs}_3\text{Sb}_2\text{I}_9$, AgBiI_4 , and BiOI , while we pursued the integral double-gate approach (Note S7, Supporting Information) for $\text{Rb}_3\text{Sb}_2\text{I}_9$ due to the weaker current tails observed in this case (Figure 3b).

The PICTS spectra generally present a peak for each distinct defect level and are parametrized with respect to the so-called rate window e^* (whose values are indicated through the color bars in Figure 4a), a key quantity used in their computation (details in Note S7, Supporting Information). Specifically, the i -th peak of one such spectrum is maximum at a temperature $T_{\text{M},i}$ at which the associated defect level has an emission rate equal to the rate window: $e_{\text{DL},i}(T_{\text{M},i}) = e^*$ (Note S7, Supporting Information). By tracking the position of a given peak for different rate window values, we systematically determined the emission rate of the corresponding defect level as a function of temperature, $e_{\text{DL},i}(T)$. We thus derived the Arrhenius-type plot presented in Figure 4b, which represents the quantity $\ln(T^2/e_{\text{DL},i}(T))$ as a function of $1/T$, where the quantity T^2 appearing in the definition of the ordinate accounts for the temperature dependence of the product $v_{\text{th}} N_{\text{eff}}$ (Note S8, Supporting Information). Each set of data points in this plot corresponds to a peak of the PICTS spectra (except for the peak $P\#$ associated with $\text{Rb}_3\text{Sb}_2\text{I}_9$; see Note S9, Supporting Information) and is therefore labeled accordingly.

All sets of data points in the Arrhenius-type plot in Figure 4b exhibit a good match with straight-line fits. This reflects the close adherence of the variable-temperature photo-induced current transients to Equations (1)–(3), thereby further confirming that the transients originate from defect-level emptying. This enabled us to extract the energy depths $E_{\text{DL},i}$ and the capture cross-sections $\sigma_{\text{c},i}$ of the defect levels from the

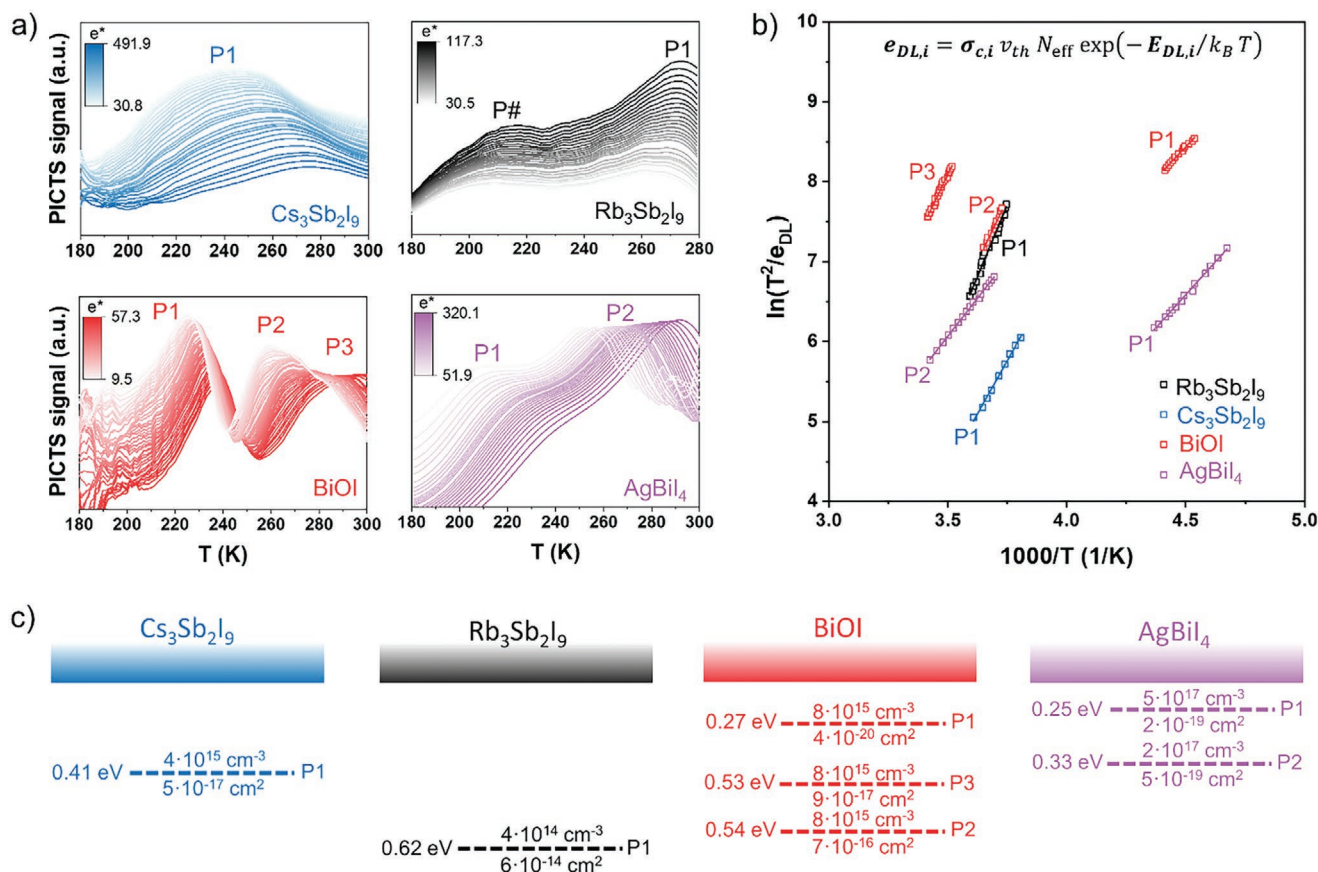


Figure 4. a) PICTS spectra of the representative PIMs. b) Arrhenius-type plot determined from the PICTS spectra in (a). c) Defect parameters extracted from the Arrhenius-type plot in (b). The bottom edge of the rectangles represents the pertinent band edge, while the dashed lines represent the detected defect levels.

slopes and vertical intercepts, respectively, of the linear interpolants (Note S8, Supporting Information). In particular, the extraction of the capture cross-sections also requires knowledge of the conductivity effective masses and density-of-states effective masses of the PIMs, which we calculated as detailed in Note S10 (Supporting Information; see also Tables S3 and S4 for the effective mass values). Based on the consistency of the Arrhenius-type plot with the defect-level emptying model in Equations (1)–(3), we could determine the volumetric concentration $N_{DL,i}$ of the corresponding defect levels by integrating the associated component of the photoinduced current transients:

$$N_{DL,i} = \int_{t_p}^{+\infty} i_{DL,i}(\tau)/qV d\tau \quad (4)$$

(see additionally Note S11, Supporting Information, for the $\text{Cs}_3\text{Sb}_2\text{I}_9$ case).

Based on the experiments, models, and analysis presented above, we could quantify the defect parameters of the four representative PIMs (Figure 4c as well as Table S5, Supporting Information), thereby demonstrating the wide applicability of PICTS for the defect-level characterization of such materials. In regard to their capture cross-sections, we extracted the values corresponding to electron capture as well as hole capture (Table S5,

Supporting Information), thus taking into account the differences in the hole and electron effective masses. For the sake of simplicity, in the following discussion we concentrate on the capture cross-section values extracted based on the assumption of electron capture (i.e., the values shown in Figure 4c), considering that the hole-capture counterparts are within the same region and also scale accordingly (Table S5, Supporting Information).

$\text{Cs}_3\text{Sb}_2\text{I}_9$ and $\text{Rb}_3\text{Sb}_2\text{I}_9$ devices featured a single defect level each. The defect level in 0D $\text{Cs}_3\text{Sb}_2\text{I}_9$ (P1 in Figure 4b,c) was at a depth of 0.41 eV and had a capture cross section of $5 \times 10^{-17} \text{ cm}^2$, which is indicative of a neutral character.^[86] By contrast, the defect level identified in two-dimensional $\text{Rb}_3\text{Sb}_2\text{I}_9$ (P1 in Figure 4b,c) was deeper (i.e., it was located 0.62 eV away from the relevant band edge) and had a considerably larger capture cross-section of $6 \times 10^{-14} \text{ cm}^2$, thereby revealing a somewhat coulombically attractive character.^[86] As for the bismuth-based PIMs examined herein, their defect-level landscape was somewhat more complex. On the one hand, for the case shown in Figure 4, BiOI presented three different defect levels: a shallow one (P1 in Figure 4b,c) with an energy depth of 0.27 eV and a capture cross-section as small as $4 \times 10^{-20} \text{ cm}^2$, which is indicative of a coulombically repulsive character;^[86] and two levels at 0.53–0.54 eV (P2 and P3 in Figure 4b,c) presenting capture cross-sections in the 10^{-17} – 10^{-16} cm^2 range, which denotes a

neutral character. On the other hand, AgBiI₄ featured two shallower defect levels—one at 0.25 eV (P1 in Figure 4b,c) and the other at 0.33 eV (P2 in Figure 4b,c)—both with capture cross-sections in the 10⁻¹⁹ cm² range or smaller, thereby indicating a coulombically repulsive character.

In regard to the defect-level concentrations, we found values in the 10¹⁴–10¹⁷ cm⁻³ range across all PIMs. The defect level in Rb₃Sb₂I₉ had the lowest concentration (4 × 10¹⁴ cm⁻³), while those in Cs₃Sb₂I₉ and BiOI had concentrations in the 10¹⁵ cm⁻³ range. Finally, a considerably higher concentration—in the 10¹⁷ cm⁻³ range—was found in AgBiI₄.

To appraise the accuracy of the extracted defect parameters, we calculated the uncertainty associated with the application of Equations (2)–(4) to the measured PICTS data (Table S5, Supporting Information). We found that the uncertainty in the extracted defect energies is on average equal to 25 meV across all sample types and smaller than 60 meV in all cases (Table S5, Supporting Information). Moreover, the uncertainty associated with the extraction of the capture cross-sections and volumetric concentrations is on average within a factor of 2–4 and generally smaller than one order of magnitude—i.e., a comparatively narrow range considering the ≈10 orders of magnitude over which these parameters may vary.

We additionally observed good consistency in the PICTS-determined defect parameters from different samples of each PIM. Specifically, energy depth differences were smaller than 90 meV, while capture cross-sections and volumetric concentrations were within the same order of magnitude (Figures S4–S7, Supporting Information). Such defect parameter variations are comparatively modest with respect to the overall ranges over which the defect parameters may vary. In addition to the uncertainty associated with the parameter extraction (see above), these variations would reflect the stoichiometric and microstructural variations commonly found in polycrystalline PIMs deposited at low temperatures, which are expected to have an impact on their defect properties. In light of this, it is not surprising that PICTS can also detect specific defect levels that may manifest only in some samples of a given material. Indeed, this was the case for BiOI samples (Figure S6d–f, Supporting Information): in addition to the levels presented in Figure 4c, some BiOI samples manifested a level with an energy depth of 0.74 eV and a capture cross-section in the 10⁻¹³ cm² range (i.e., with a coulombically attractive character). This indicates that variations may occur in the preparation of BiOI samples that may or may not lead to the formation of such a defect level.

While in principle the defect levels detected in a PICTS experiment may originate from any of the semiconducting layers in the device stack, our PICTS implementation has a dramatically larger selectivity toward the defect levels of the PIM layer (in contrast to techniques such as DLTS, TAS, and I-DLTS). First, defect-level filling in such experiments relies on the absorption of photons with energy slightly above the bandgap of the PIMs (i.e., photons with energy much lower than the bandgap of the charge transport layers), hence by far primarily absorbed by the PIMs themselves (cf., in DLTS, TAS, and I-DLTS, charges for defect-level filling are supplied from the electrodes or layers within the device stack). Additionally, due to its thickness, the PIM layer contributes at least

a one-order-of-magnitude larger share of the volume between the device electrodes, which further enhances the selectivity of PICTS toward the defect levels in the PIM. In fact, PICTS inherently provides a straightforward route to assessing if the observed photoinduced current transients may reflect the defect properties of the transport layers. This involves a comparative analysis of the PICTS-determined defect levels from device stacks that differ either in the PIM or the charge transport layers. For instance, while the Cs₃Sb₂I₉ and Rb₃Sb₂I₉ devices presented in Figure 4c both comprise a poly-TPD hole-transport layer (HTL), their defect levels are utterly distinct. This allows us to conclude that their poly-TPD HTL does not contribute to the PICTS-determined defect levels of these Cs₃Sb₂I₉ and Rb₃Sb₂I₉ devices. Along the same lines, while the Rb₃Sb₂I₉ and AgBiI₄ devices presented in Figure 4c both comprise a compact TiO₂ (c-TiO₂) electron-transport layer (ETL), no similarity is found in their defect levels. This rules out that their c-TiO₂ ETLs have an impact on their PICTS-determined defect levels. Moreover, c-TiO₂/AgBiI₄/Spiro-OMeTAD devices (Figure 4c) manifest defect parameters that directly relate to those of mp-TiO₂/AgBiI₄/poly-TPD devices (mp-TiO₂: mesoporous TiO₂; see Figure S8, Supporting Information), and utterly distinct from those of mp-TiO₂/Cs₃Sb₂I₉/poly-TPD devices (Figure 4c). Overall, this allows us to rule out that the defect parameters obtained from Cs₃Sb₂I₉, Rb₃Sb₂I₉, and AgBiI₄ devices originate from their transport layers. Ultimately, this illustrates the selectivity of PICTS toward the defect levels in the photoactive layers of PIM solar cells as well as the straightforward manner in which such selectivity can be experimentally verified.

2.3. One-Center Defect Tolerance Analysis (OCDTA)

Although the widely accepted notion of defect tolerance makes direct reference to defect levels that are shallow or with small capture-cross sections, no straightforward quantitative criterion has been formulated to date that allows the identification of a defect tolerant semiconductor based on the energy depth and capture cross-section values of its defect levels. Therefore, as a preliminary and qualitative assessment of the defect tolerance of the PIMs investigated herein, we considered comparing their PICTS-determined defect parameters with those reported in the literature on lead-halide perovskites, which are widely regarded as the paragon of defect tolerant semiconductors. We thus found that the defect parameters of the PIMs considered herein (Figure 4) fall within the ranges also reported for polycrystalline lead-halide perovskites (Table S6, Supporting Information). Therefore, this preliminary comparison does not suggest that the antimony- and bismuth-based PIMs considered herein are generally “worse off” in terms of defect tolerance than the lead-based perovskite counterparts.

Looking beyond the limits of the current definition of defect tolerance and the preliminary comparison above, we reasoned that the quantitative evaluation of the defect tolerance of a semiconductor would require the contextualization of its defect properties within the intended device application and the relevant boundary conditions. Photovoltaics offers an obvious example: the capture and emission rates of a defect level in a

semiconductor—i.e., the key quantities determining the impact of a defect level on photovoltaic performance—depend not only on the corresponding defect parameters but also on the photo-generation rate. Therefore, a semiconductor may or may not be tolerant to one of its defects depending also on whether, for example, it absorbs sunlight more or less strongly, or, as another example, if it is used for outdoor solar photovoltaics or indoor photovoltaics. In other words, while the defect parameter values play an essential role in determining the defect tolerance of a semiconductor, the quantitative assessment of defect tolerance cannot be abstracted from the overall “system” (i.e., the device and its operating conditions) in which the semiconductor is placed.

Based on the above considerations, we developed a methodology that quantifies the defect tolerance of a PIM in relation to the two key determinants of its photovoltaic efficiency, i.e., the short-circuit current and the open-circuit voltage. We refer to this methodology as OCDTA because it evaluates the defect tolerance of a PIM in relation to each individual defect level (i.e., center). In particular, OCDTA assesses the impact of each level (with concentration $N_{DL,i}$ and capture cross-section $\sigma_{c,i}$) through two metrics, referred to as *one-center external quantum efficiency* (EQE) and *one-center open-circuit voltage deficit*, which are defined as follows, respectively (details in Note S12, Supporting Information)

$$EQE_{0,DL,i} = \frac{2\mu|V_{bi}|}{L^2} \frac{1}{N_{DL,i}\sigma_{c,i}\nu_{th}} \left(1 - \exp\left(-\frac{L^2}{2\mu|V_{bi}|} N_{DL,i}\sigma_{c,i}\nu_{th}\right) \right) \quad (5)$$

$$\Delta V_{oc,nr,i} = \frac{k_B T}{q} \ln\left(\frac{1}{2p_e} \frac{2Bn + N_{DL,i}\sigma_{c,i}\nu_{th}}{Bn}\right) \quad (6)$$

Here, μ is the average carrier mobility in the PIM, $|V_{bi}|$ is the magnitude of the built-in voltage of the PIM device, p_e is the outcoupling efficiency, B is the radiative recombination coefficient, n is the mobile carrier density, and all the other parameters are as defined earlier. The significance of $EQE_{0,DL,i}$ and $\Delta V_{oc,nr,i}$ lies in the fact that they quantify the impact of a defect level on the short-circuit EQE (which directly relates to the short-circuit current density) and the open-circuit voltage deficit due to nonradiative recombination, respectively, if carrier capture associated with that defect level is rate-setting in terms of the overall recombination kinetics.

Building on Equations (5) and (6) and through the algorithms detailed in Notes S12–S14 and Figures S9 and S10 (Supporting Information), OCDTA allows the straightforward determination of $EQE_{0,DL,i} = EQE_{0,DL,i}(\mu)$ and $\Delta V_{oc,nr,i} = \Delta V_{oc,nr,i}(n)$ based only on the following input quantities: the PICTS-determined defect parameters; the effective masses of the PIM; and the optical absorption spectrum of the PIM. For the sake of comparison, we additionally carried out the same analysis on MAPbI₃, using literature values of the relevant quantities (see also Table S6–S8, Supporting Information).^[25,32,87,88]

As a general trend, the one-center EQE associated with all defect levels monotonically increases with the carrier mobility and eventually saturates (Figure 5), consistent with the physical picture that a high mobility allows a larger fraction of photocarriers to escape recombination. Moreover, the one-center $\Delta V_{oc,nr}$

monotonically decreases with carrier density (Figure 5), consistent with the concurrent reduction in the weight of the nonradiative recombination.

In regard to Cs₃Sb₂I₉ and AgBiI₄, their defect levels would have minimal impact on the EQE across the entire mobility range considered (Figure 5a,d). Indeed, the defect levels detected in Cs₃Sb₂I₉ and AgBiI₄ have comparatively small capture cross-sections, leading to a smaller impact on the carrier collection length (Note S12, Supporting Information). At the same time, these levels lead to a reduction of the one-center open-circuit voltage by an amount of ≈ 0.45 and ≈ 0.40 V, respectively, over the carrier density range generally relevant to solar cell operation (see shading in the corresponding plots in Figure 5a,d; see also Note S15 and Figure S11, Supporting Information). This indicates that, while the defect levels detected in AgBiI₄ have by far the largest concentrations of all four PIMs investigated herein, in fact, these levels would have a comparatively small effect on the $\Delta V_{oc,nr,i}$ due to their rather low capture cross-sections. As for Rb₃Sb₂I₉, the impact of its defect level would be appreciably larger, leading to a pronounced reduction in EQE and a higher open-circuit voltage deficit (Figure 5b). This can be ascribed to the considerably larger capture cross-section of its defect level. Finally, BiOI presents a particularly interesting case (Figure 5c): the levels presented in Figure 4c would have no detrimental impact on the EQE in the relevant mobility range, while its levels with an energy depth of ≈ 0.53 eV (P2 and P3 of Figure 4) would cause a larger $\Delta V_{oc,nr,i}$ of ≈ 0.55 V. If we additionally consider the deeper level at 0.74 eV detected in some of the BiOI samples (Figure S6, Supporting Information), the situation would change significantly due to the large capture cross-section of this level: the one-center EQE would be appreciably reduced (note, however, the uncertainty in the mobility range, which has not been extensively characterized), while the maximum $\Delta V_{oc,nr,i}$ would rise to ≈ 0.7 V (Figure S12, Supporting Information).

Interestingly, a comparison with the plots obtained for MAPbI₃ (Figure 5e) reveals that the one-center EQE traces of the representative PIMs are globally (i.e., at any given value of the carrier mobility) at a similar level (BiOI and Rb₃Sb₂I₉ case) or superior (Cs₃Sb₂I₉ and AgBiI₄ cases) to those of MAPbI₃. However, by considering the mobility range reported in the literature for all of these materials (see shading in the corresponding plots in Figure 5),^[11,26,44,59–62,89] it becomes apparent that, while the defect parameters of MAPbI₃ are not “better off” (in terms of depth and capture cross-section) than those of the representative PIMs, their impact on the carrier collection length (Note S12, Supporting Information) and the one-center EQE of MAPbI₃ would be minimal due to the comparatively large mobility of MAPbI₃. Nonetheless, all of the PIMs would be tolerant to their defect levels presented in Figure 4 in terms of photoconversion at short circuit. The only exception concerns the deep level detected in some of the BiOI samples (Figure S12, Supporting Information), to which BiOI would not be tolerant in solar cells at short circuit.

In terms of the open-circuit voltage deficit, the defect levels in MAPbI₃ would globally lead to a $\Delta V_{oc,nr}$ comparable to that of Cs₃Sb₂I₉ and AgBiI₄, given that the corresponding $\Delta V_{oc,nr} - n$ traces are nearly overlapping. Interestingly, this is in spite of the

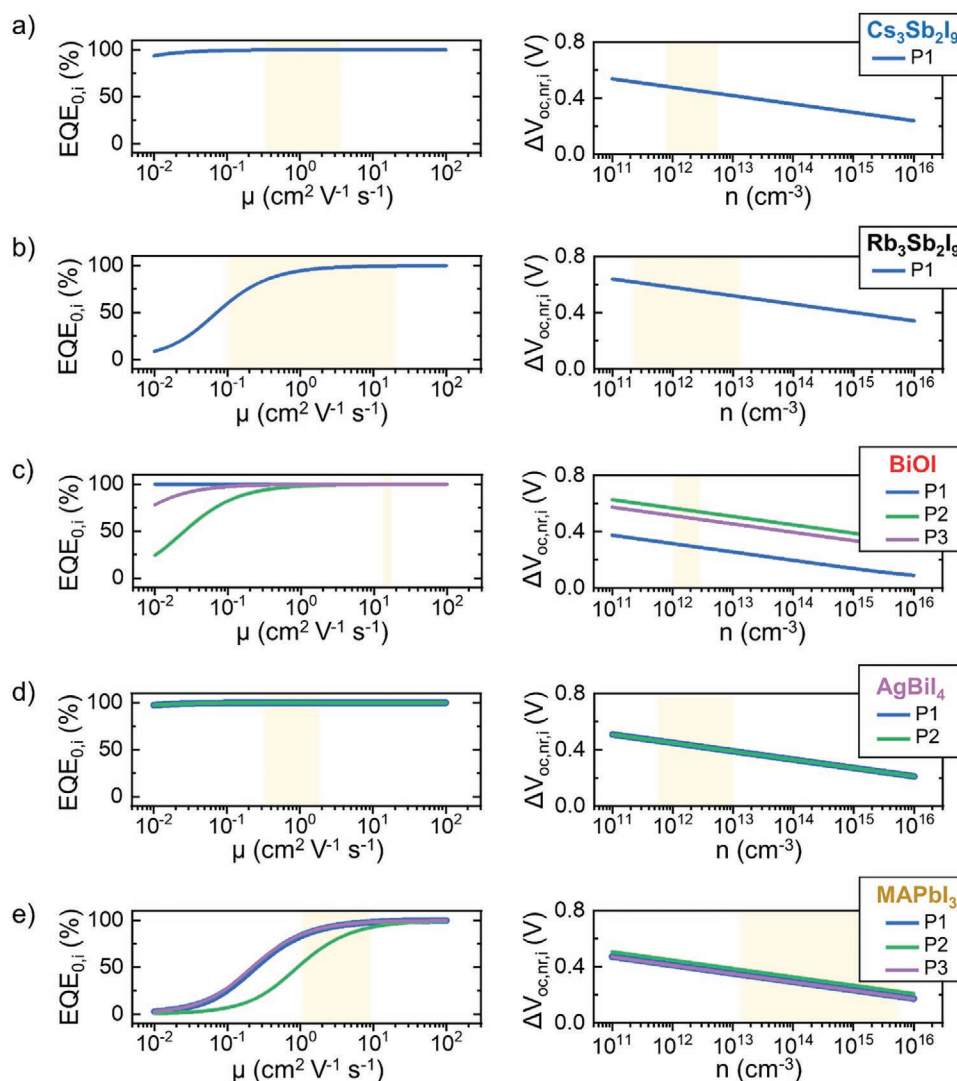


Figure 5. One-center EQE and one-center open-circuit voltage deficit associated with a) $\text{Cs}_3\text{Sb}_2\text{I}_9$, b) $\text{Rb}_3\text{Sb}_2\text{I}_9$, c) BiOI , and d) AgBiI_4 , as determined via OCDTA using the defect parameters presented in Figure 4. e) One-center EQE and one-center open-circuit voltage deficit associated with MAPbI_3 , as determined via OCDTA using the defect parameters reported by Heo et al.^[87] The shaded areas in the one-center EQE plots correspond to the mobility ranges reported in the literature for relevant compounds (see also Table S8, Supporting Information).^[11,26,44,59–62,89] The shaded areas in the one-center open-circuit voltage deficit plots are obtained as detailed in Note S15 and Figure S11 (Supporting Information).

larger capture cross-sections of some of the defects in MAPbI_3 (Table S6, Supporting Information), whose impact is reduced due to a larger carrier concentration in the corresponding devices. Owing to the low capture cross-sections of its defect levels, the AgBiI_4 case at open circuit would not be considerably different from MAPbI_3 , denoting acceptable tolerance of AgBiI_4 to its detected defect levels. By contrast, $\text{Cs}_3\text{Sb}_2\text{I}_9$, $\text{Rb}_3\text{Sb}_2\text{I}_9$, and BiOI are considerably less tolerant to their defect levels at open circuit compared to the MAPbI_3 case.

In summary, based on the quantitative insight provided by OCDTA, AgBiI_4 is expected to be comparatively tolerant to its defect levels we detected by PICTS. Therefore, rather than prioritizing the reduction of the concentrations of these levels, future efforts aiming to boost the photovoltaic performance of AgBiI_4 should focus on device and materials aspects such as

interfaces, charge transport layers, and excitonic effects. On the other hand, $\text{Rb}_3\text{Sb}_2\text{I}_9$ and BiOI exhibit lower defect tolerance (particularly at open circuit), in part due to the larger capture cross-sections of their defect levels. In the case of BiOI , a particularly detrimental defect level was detected in some of the samples. Consequently, identifying the origin of this level is the worthwhile goal of future studies. Additionally, the photovoltaic impact of the PICTS-determined level of $\text{Cs}_3\text{Sb}_2\text{I}_9$ would be intermediate between that of AgBiI_4 and $\text{Rb}_3\text{Sb}_2\text{I}_9$ or BiOI , reflecting its intermediate capture cross-section value. Finally, PICTS and OCDTA jointly revealed that PIMs may in fact possess more benign defect levels (shallower or with smaller capture cross-sections) than MAPbI_3 , but their defect tolerance could be lower because of their smaller mobility and due to their operating conditions within solar cells.

2.4. Broader Potential of PICTS for the Defect Characterization of PIMs and Related Absorbers

To evaluate the broader potential of PICTS in PIM/perovskite photovoltaics research, it is important to identify its ultimate limits in terms of the smallest concentration and the largest energy depth of the defect levels that it can probe. To the best of our knowledge, these limits have not been examined to date in the context of PIM/perovskite photovoltaics, nor can they be inferred from the earlier PICTS literature, which covers other material systems and device configurations.

The ability of PICTS to detect a defect level in a PIM/perovskite solar cell is ultimately limited by the strength of the defect-level-emptying current in comparison to the magnitude of the background noise. Based on the model for the defect-level-emptying current in Equation (1) and considering the shot noise and Johnson-Nyquist noise present in PIM/perovskite solar cells,^[26,90,91] we derived that the ultimate sensitivity of PICTS for the investigation of defect levels in PIM/perovskite solar cells can be expressed as (Note S16, Supporting Information):

$$N_{DL,i} \geq \frac{C(T)}{\sqrt{\sigma_{c,i}} \exp(-E_{DL,i}/2k_B T)} \quad (7)$$

Here, $C(T)$ is a quantity that aggregates device and materials parameters (Note S16, Supporting Information), including the effective masses of the absorber, as well as the shunt resistance and dark current of the corresponding solar cells.

To appraise the implications of Equation (7), we determined the parameters in question for the representative PIMs investigated in this study (Tables S3, S4, and S9, Supporting Information). Specifically, **Figure 6** shows the corresponding color maps derived from Equation (7) for the case of BiOI at both 300 K and 180 K (i.e., at the maximum and minimum temperatures of the PICTS experiments discussed earlier). Each point of these color maps is associated with a pair of energy depth and capture cross-section values of a hypothetical defect level, while the corresponding color indicates the minimum defect concentration that PICTS could detect.

A comparison of the plots in Figure 6 reveals that, within the temperature range probed in this study, it is at 300 K that PICTS

can detect deeper defect levels. This reflects the dominance of the emission rate (Equation 3) in the temperature dependence of the signal-to-noise ratio (Equation 7) in PIM solar cells (as we also observed in other PIMs). We thus focus on the plot at 300 K to gain quantitative insight into the detection limits of PICTS for the case of BiOI (see Figure S13, Supporting Information, for all other representative PIMs). Figure 6b shows that the lowest defect levels that could be detected would have an energy depth appreciably greater than 1.0 eV (i.e., down to mid-gap for BiOI). If we specifically focus on the defect levels with an energy depth of 0.6 eV (in line with the deeper defect levels detected across all representative PIMs examined herein), we find that PICTS could reveal a concentration of neutral defect levels below $1 \times 10^{12} \text{ cm}^{-3}$ (Figure 6b). Given that the atomic concentration of BiOI is of $\approx 10^{22} \text{ cm}^{-3}$, this highlights a remarkable sensitivity of PICTS applied to PIM solar cells down to the part-per-trillion range. Additionally, this provides a reality check on the defect level concentrations we detected experimentally, which are larger than this ultimate limit, as indeed expected.

In regard to the ability of PICTS to detect shallow levels, the plots in Figure 6 reveal that PICTS has in principle a higher sensitivity for smaller energy depths. However, shallow levels may give rise to rather short transients (in view of their larger emission rates) at comparatively high temperatures. Therefore, the detection of shallow levels generally requires running PICTS at sufficiently low temperatures, thus allowing the corresponding deep-level-emptying transients to be “stretched” in time. For instance, the shallower levels of AgBiI_4 and BiOI (Figure 4a,c) were detected at comparatively low temperatures. Specifically, the minimum energy depth that can be probed in a PICTS experiment depends on the minimum temperature used, which may be determined by practical factors involving the experimental setup, the measuring time, and the materials used.

We emphasize that the detection limits just discussed are not the general sensitivity limits of PICTS, but are specific to absorbers such as PIMs and their thin-film solar cells, as Equation (7) also accounts for materials and device properties. Therefore, the above sensitivity analysis confirms the potential of PICTS to be widely applied for the in situ characterization of defect levels in PIM thin films embedded within solar cells with concentrations down to the part-per-trillion range as well as energy depths larger

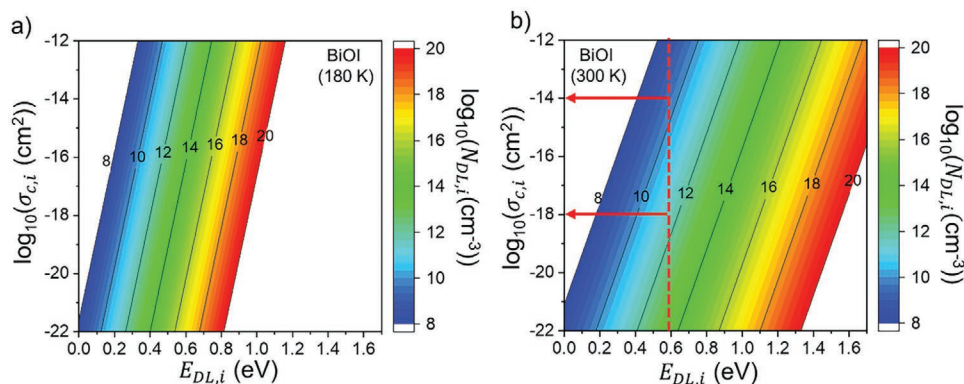


Figure 6. Sensitivity of PICTS applied to PIM solar cells. The case of BiOI devices is shown here. a) Sensitivity at 180 K. b) Sensitivity at 300 K. The contour line labels indicate the logarithm base 10 of the minimum defect concentration that can be detected. The dashed line and arrows in (b) refer to the case of a neutral defect level with an energy depth of 0.6 eV.

than 1.0 eV. Considering their materials and device similarity with PIMs, our analysis also suggests the applicability of PICTS to related emerging absorbers such as mainstream lead-halide perovskites. In fact, given that the defect characterization of lead-halide perovskites through conventional capacitance-based techniques has been recently brought into question,^[66,67] the sensitivity analysis presented herein points to the opportunity that PICTS could also provide for gaining insight into the defect properties of mainstream lead-halide perovskites.

3. Conclusion

In this work, we established, for the first time, the wide applicability of PICTS for the in situ assessment of the defect parameters (i.e., energy depths, capture cross-sections, and concentrations) of lead-free PIMs, which have recently attracted a considerable amount of attention in photovoltaics research. While mainstream defect spectroscopies would be problematic or inapplicable to PIMs due to the near-intrinsic character of many such absorbers, herein we successfully conducted a PICTS investigation of four representative PIMs— $\text{Cs}_3\text{Sb}_2\text{I}_9$, $\text{Rb}_3\text{Sb}_2\text{I}_9$, AgBiI_4 , and BiOI —embedded within thin-film solar cells. We found that these absorbers present defect levels with energy depths in the range of 0.3–0.7 eV, with one single defect level being dominant in $\text{Cs}_3\text{Sb}_2\text{I}_9$ and $\text{Rb}_3\text{Sb}_2\text{I}_9$, and with AgBiI_4 and BiOI presenting multiple defect levels. Additionally, while all defect levels in $\text{Cs}_3\text{Sb}_2\text{I}_9$ and AgBiI_4 and the shallower levels in BiOI manifested rather small capture cross-sections—denoting a neutral or coulombically repulsive nature—much larger capture-cross-section values were found for the defect level in $\text{Rb}_3\text{Sb}_2\text{I}_9$ and the deepest level in BiOI .

Building on such insight, we developed a methodology, called One-Centre Defect Tolerance Analysis (OCDTA), to quantitatively assess the defect tolerance of PIMs in the photovoltaics context. This analysis revealed that AgBiI_4 would be rather tolerant to the defect levels detected by PICTS, while $\text{Cs}_3\text{Sb}_2\text{I}_9$ and, to a greater extent, $\text{Rb}_3\text{Sb}_2\text{I}_9$ and BiOI would be particularly affected by their PICTS-determined defect levels.

Finally, we provided quantitative insight into the broader potential of PICTS for the defect characterization of PIMs and related absorbers such as mainstream halide perovskites, revealing that this technique can probe defect levels down to mid-gap and can reach a sensitivity in the part-per-trillion range.

In view of its experimental simplicity, wide applicability, and high sensitivity, PICTS has significant potential to become a standard technique to further the understanding of the defect properties of PIMs as well as their lead-halide perovskite counterparts. In fact, PICTS and OCDTA could help identify the compositions and processing conditions conducive to more benign defect properties or superior defect tolerance, thereby catalyzing the development of easy-to-make materials for next-generation photovoltaics.

4. Experimental Section

XRD Characterization: XRD patterns were collected on thin films of $\text{Cs}_3\text{Sb}_2\text{I}_9$, $\text{Rb}_3\text{Sb}_2\text{I}_9$, and AgBiI_4 deposited on glass substrates with

a protective covering of poly(methyl methacrylate) (PMMA). The instrument used was a Bruker D8 diffractometer (Cu $K\alpha$ radiation, $\lambda = 1.541 \text{ \AA}$) with an Oxford Cryosystems Phenix variable-temperature sample stage. The sample space was evacuated and the stage was cooled at 1 K min^{-1} to 180 K and allowed to thermalize for one hour. Subsequently, XRD scans were collected at 10 K increments from 180 to 300 K, with heating rate 1 K min^{-1} and 10 minutes thermalization time at each temperature before taking the measurement. Scans were collected in the range $10 \leq 2\theta(^{\circ}) \leq 60$ with a step size of 0.02° and collection time 0.5 s per step.

SEM Characterization: The SEM images of $\text{Cs}_3\text{Sb}_2\text{I}_9$, $\text{Rb}_3\text{Sb}_2\text{I}_9$, and AgBiI_4 were acquired using a Zeiss GeminiSEM 500 scanning electron microscope with an accelerating voltage of 10 kV (pressure of 2×10^{-5} mbar). The SEM image of BiOI was taken using an FEI Magellan (XHR 400L) scanning electron microscope using an accelerating voltage of 10 kV (pressure of 10^{-5} mbar).

UV-Vis Spectrophotometry: The absorption coefficients of $\text{Cs}_3\text{Sb}_2\text{I}_9$, $\text{Rb}_3\text{Sb}_2\text{I}_9$, and AgBiI_4 were calculated as $\alpha = -\ln(T/(1-R))/L$. L is the PIM film thickness (measured with a D-100 Stylus Profliometer, KLA-Tencor) in samples comprising PIM thin films on glass substrates, and T and R are their transmittance and reflectance (measured with a PerkinElmer LAMBDA 950 UV-Vis-NIR spectrophotometer), respectively.

UPS Characterization: UPS spectra were acquired on AgBiI_4 thin films using a Kratos Ultra DLD ultraviolet photoelectron spectrometer, which featured a monochromatic He I (21.2 eV) excitation source.

$\text{Cs}_3\text{Sb}_2\text{I}_9$, $\text{Rb}_3\text{Sb}_2\text{I}_9$, and BiOI Device Fabrication: $\text{Cs}_3\text{Sb}_2\text{I}_9$, $\text{Rb}_3\text{Sb}_2\text{I}_9$, and BiOI devices were fabricated according to the procedures reported in refs. [60,62], and [59], respectively (see Note S2, Supporting Information, for details).

AgBiI_4 Device Fabrication: Fluorine-doped tin-oxide (FTO)/glass substrates were cleaned and then coated with a c- TiO_2 film as detailed in Ref. [26]. All subsequent fabrication steps were performed in an N_2 -filled glove box, unless noted otherwise. AgI and BiI_3 powders were mixed (1:1 molar ratio) in dimethylsulfoxide:dimethylformamide (1:3 volume ratio), targeting a solution concentration of 0.4 M. The solution was stirred for 4 hours at room temperature and then filtered with a $0.22 \mu\text{m}$ PTFE filter. The solution was then spin-coated on c- TiO_2 /FTO substrates (6000 rpm, 30 s); 18 s into the spin-coating cycle, chloroform (150 μL) was dispensed onto the substrate. Subsequently, samples were annealed at 100°C ; then, their temperature was raised to 180°C (over 10 min) and finally kept at 180°C (for 10 min). Spiro-OMeTAD was then spin-coated on the AgBiI_4 thin films from a chlorobenzene solution according to the procedure detailed in Ref. [26]. Finally, 100 nm thick silver electrodes were thermally evaporated in high vacuum through a shadow mask, defining a device active area of 7.25 mm^2 .

AgBiI_4 devices comprising an mp- TiO_2 layer were also fabricated. In such a case, device fabrication was conducted as above, except for the following steps: after the deposition of a c- TiO_2 film, an mp- TiO_2 layer was deposited as detailed in ref. [60]; the spiro-OMeTAD film was replaced with a poly-TPD film, which was spin-coated from a chlorobenzene solution (10 mg mL^{-1}) according to the procedure detailed in ref. [60].

EQE Characterization: EQE measurements were carried out using a Keithley 6420 source-measure unit (Tektronix) and a monochromated light source (Zolix Omni- λ 2005i) calibrated with a power meter assembly (Thorlabs PM200 and Thorlabs S120VC).

PICTS: The PIM devices were mounted in a cryostat (CRYO Industries of America) equipped with an optical window. After the sample chamber was evacuated, the sample was cooled to the desired temperature (180 K) using a liquid-helium closed-cycle refrigerator system. The sample temperature was then raised at a rate of 1 K min^{-1} up to 300 K. The sample temperature was controlled using a Model 335 Cryogenic Temperature Controller (Lakeshore). Suitable light pulses (see below) were concurrently applied. The corresponding current signal from the PIM devices was amplified with a DHPA-100 amplifier (FEMTO), whose output was digitized and acquired through a Multifunction I/O National Instrument Device controlled via a custom LabVIEW program. The PIM devices were maintained with 0 V across and were illuminated from their FTO or ITO

electrodes. The BiOI and AgBiI₄ devices were illuminated using an Osram LA CN5M LED (dominant wavelength of 617 nm) with an irradiance of 279 μW cm⁻² and 530 μW cm⁻², respectively. The Cs₃Sb₂I₉ and Rb₃Sb₂I₉ devices were illuminated using an Osram LY CP7P LED (dominant wavelength of 590 nm) with an irradiance of 44 μW cm⁻² and 62 μW cm⁻², respectively. The duration of the light pulses was 1.0 s for Cs₃Sb₂I₉ and Rb₃Sb₂I₉ devices, 1.5 s for BiOI devices, and 1.1 s for AgBiI₄ devices.

Density Functional Theory Calculations: The total energy of the system and the band energies were determined using the Vienna Ab Initio Simulation Package (VASP version 5.4.1).^[92] Exchange-correlation effects were treated with the Perdew–Burke–Ernzerhof (PBE) functional.^[93] Standard PAW potentials were used for the core-electrons of the atoms.^[94] A plane-wave basis with an energy cutoff (E_{cut}) was used based on the standard choice determined by the elements involved with E_{cut} ranging from 220 to 250 eV. A converged K-point mesh was used for initial coordinate, volume, and charge density optimizations. To test the sensitivity of the effective mass results, a second set of calculations was performed fixing the atoms, volume, and charge density but using the LDA functional^[95] instead of the PBE functional in the final band energy calculations.

Supporting Information

Supporting Information is available from the Wiley Online Library or from the author.

Acknowledgements

V.P. acknowledges financial support from the National Natural Science Foundation of China (61950410759 and 61805166), the Jiangsu Province Natural Science Foundation (BK20170345), the Collaborative Innovation Center of Suzhou Nano Science & Technology, the Priority Academic Program Development of Jiangsu Higher Education Institutions (PAPD), the 111 Project, and the Joint International Research Laboratory of Carbon-Based Functional Materials and Devices. R.L.Z.H. acknowledges support from the Royal Academy of Engineering via the Research Fellowship program (RF\201718\1701). J.L.M.-D. thanks the Royal Academy of Engineering grant, CiET, 1819_24. The authors are thankful to Vladimir Kremnican for his technical support with the PICTS apparatus.

Conflict of Interest

The authors declare no conflict of interest.

Author Contributions

V.P. conceived and led the project, designed the experiments, wrote the manuscript, constructed the PICTS setup, established the PICTS measurement protocol and data analysis routine, analyzed the PICTS data, developed the models for the PICTS transients, developed the one-center defect tolerance analysis, and developed the model for and calculated the sensitivity of PICTS for the characterization of PIM solar cells. J.Z. and C.K. carried out the PICTS experiments and the associated data processing routine (under the supervision of V.P.). J.Z. deposited the AgBiI₄ thin films, fabricated the corresponding devices, and measured the photoresponse stability and the I - V characteristics of all device types (under the supervision of V.P.). B.R.T. calculated the band energies and effective masses of the PIMs. J.M., F.L., and Y.P. deposited the Cs₃Sb₂I₉ and Rb₃Sb₂I₉ thin films and fabricated the corresponding devices (under the supervision of V.P.). J.M. measured the transmittance and reflectance of Cs₃Sb₂I₉, Rb₃Sb₂I₉, and AgBiI₄ films, and characterized their morphology and composition (under the supervision of V.P.). T.N.H. grew the BiOI thin films, characterized their morphology and

phase purity, and fabricated the corresponding devices (under the supervision of R.L.Z.H.). N.D.K. characterized the structural stability of all materials via variable-temperature XRD (under the supervision of S.E.D.). K.X. contributed to the construction of the PICTS setup (under the supervision of V.P.). H.S. contributed to the original design of the study and commented on the manuscript. All authors discussed the results and revised the manuscript.

Data Availability Statement

The data that support the findings of this study are available from the corresponding author upon reasonable request.

Keywords

antimony-based perovskites, bismuth-based perovskites, defect tolerance, lead-free perovskite-inspired materials, nonradiative recombination, PICTS, solar cells

Received: December 26, 2020

Revised: March 12, 2021

Published online: May 4, 2021

- [1] P. K. Nayak, S. Mahesh, H. J. Snaith, D. Cahen, *Nat. Rev. Mater.* **2019**, *4*, 269.
- [2] A. K. Jena, A. Kulkarni, T. Miyasaka, *Chem. Rev.* **2019**, *119*, 3036.
- [3] J. Zhou, J. Huang, *Adv. Sci.* **2018**, *5*, 1700256.
- [4] Q. Van Le, H. W. Jang, S. Y. Kim, *Small Methods* **2018**, *2*, 1700419.
- [5] V. Pecunia, *J. Phys. Mater.* **2019**, *2*, 042001.
- [6] X.-J. She, C. Chen, G. Divitini, B. Zhao, Y. Li, J. Wang, J. F. Orri, L. Cui, W. Xu, J. Peng, S. Wang, A. Sadhanala, H. Siringhaus, *Nat. Electron.* **2020**, *3*, 694.
- [7] R. E. Brandt, J. R. Poindexter, P. Gorai, R. C. Kurchin, R. L. Z. Hoye, L. Nienhaus, M. W. B. Wilson, J. A. Polizzotti, R. Sereika, R. Žaltauskas, L. C. Lee, J. L. MacManus-Driscoll, M. Bawendi, V. Stevanović, T. Buonassisi, *Chem. Mater.* **2017**, *29*, 4667.
- [8] A. Walsh, A. Zunger, *Nat. Mater.* **2017**, *16*, 964.
- [9] K. X. Steirer, P. Schulz, G. Teeter, V. Stevanovic, M. Yang, K. Zhu, J. J. Berry, *ACS Energy Lett.* **2016**, *1*, 360.
- [10] E. M. Tennyson, T. A. S. Doherty, S. D. Stranks, *Nat. Rev. Mater.* **2019**, *4*, 573.
- [11] T. M. Brenner, D. a. Egger, L. Kronik, G. Hodes, D. Cahen, *Nat. Rev. Mater.* **2016**, *1*, 15007.
- [12] G. Kim, A. Petrozza, *Adv. Energy Mater.* **2020**, *10*, 2001959.
- [13] J. R. Poindexter, R. L. Z. Hoye, L. Nienhaus, R. C. Kurchin, A. E. Morishige, E. E. Looney, A. Osherov, J.-P. Correa-Baena, B. Lai, V. Bulović, V. Stevanović, M. G. Bawendi, T. Buonassisi, *ACS Nano* **2017**, *11*, 7101.
- [14] H. Tan, F. Che, M. Wei, Y. Zhao, M. I. Saidaminov, P. Todorović, D. Broberg, G. Walters, F. Tan, T. Zhuang, B. Sun, Z. Liang, H. Yuan, E. Fron, J. Kim, Z. Yang, O. Voznyy, M. Asta, E. H. Sargent, *Nat. Commun.* **2018**, *9*, 3100.
- [15] D. Meggiolaro, S. G. Motti, E. Mosconi, A. J. Barker, J. Ball, C. Andrea Riccardo Perini, F. Deschler, A. Petrozza, F. De Angelis, *Energy Environ. Sci.* **2018**, *11*, 702.
- [16] A. Babayigit, A. Ethirajan, M. Muller, B. Conings, *Nat. Mater.* **2016**, *15*, 247.
- [17] J. Li, H.-L. Cao, W.-B. Jiao, Q. Wang, M. Wei, I. Cantone, J. Lü, A. Abate, *Nat. Commun.* **2020**, *11*, 310.
- [18] J. Kang, L. W. Wang, *J. Phys. Chem. Lett.* **2017**, *8*, 489.

- [19] A. M. Ganose, C. N. Savory, D. O. Scanlon, *Chem. Commun.* **2017**, 53, 20.
- [20] Z. Xiao, Z. Song, Y. Yan, *Adv. Mater.* **2019**, 31, 1.
- [21] V. Pecunia, L. G. Occhipinti, A. Chakraborty, Y. Pan, Y. Peng, *APL Mater.* **2020**, 8, 100901.
- [22] V. Andrei, R. L. Z. Hoye, M. Crespo-Quesada, M. Bajada, S. Ahmad, M. De Volder, R. Friend, E. Reisner, *Adv. Energy Mater.* **2018**, 8, 1801403.
- [23] Y.-T. Huang, S. R. Kavanagh, D. O. Scanlon, A. Walsh, R. L. Z. Hoye, *Nanotechnology* **2021**, 32, 132004.
- [24] T. Miyasaka, A. Kulkarni, G. M. Kim, S. Öz, A. K. Jena, *Adv. Energy Mater.* **2020**, 10, 1902500.
- [25] Y. Peng, T. N. Huq, J. Mei, L. Portilla, R. A. Jagt, L. G. Occhipinti, J. L. MacManus-Driscoll, R. L. Z. Hoye, V. Pecunia, *Adv. Energy Mater.* **2021**, 11, 2002761.
- [26] V. Pecunia, Y. Yuan, J. Zhao, K. Xia, Y. Wang, S. Duhm, L. Portilla, F. Li, *Nano-Micro Lett.* **2020**, 12, 27.
- [27] H. Liang, F. Yuan, A. Johnston, C. Gao, H. Choubisa, Y. Gao, Y. Wang, L. K. Sagar, B. Sun, P. Li, G. Bappi, B. Chen, J. Li, Y. Wang, Y. Dong, D. Ma, Y. Gao, Y. Liu, M. Yuan, M. I. Saidaminov, S. Hoogland, Z. Lu, E. H. Sargent, *Adv. Sci.* **2020**, 7, 1903213.
- [28] Y. Zhang, Y. Liu, Z. Xu, H. Ye, Z. Yang, J. You, M. Liu, Y. He, M. G. Kanatzidis, S. Liu, *Nat. Commun.* **2020**, 11, 2304.
- [29] J. Luo, X. Wang, S. Li, J. Liu, Y. Guo, G. Niu, L. Yao, Y. Fu, L. Gao, Q. Dong, C. Zhao, M. Leng, F. Ma, W. Liang, L. Wang, S. Jin, J. Han, L. Zhang, J. Etheridge, J. Wang, Y. Yan, E. H. Sargent, J. Tang, *Nature* **2018**, 563, 541.
- [30] Q. Chen, J. Wu, X. Ou, B. Huang, J. Almutlaq, A. A. Zhumekenov, X. Guan, S. Han, L. Liang, Z. Yi, J. Li, X. Xie, Y. Wang, Y. Li, D. Fan, D. B. L. Teh, A. H. All, O. F. Mohammed, O. M. Bakr, T. Wu, M. Bettinelli, H. Yang, W. Huang, X. Liu, *Nature* **2018**, 567, 88.
- [31] S. Yakunin, D. N. Dirin, Y. Shynkarenko, V. Morad, I. Cherniukh, O. Nazarenko, D. Kreil, T. Nausser, M. V. Kovalenko, *Nat. Photonics* **2016**, 10, 585.
- [32] R. E. Brandt, V. Stevanović, D. S. Ginley, T. Buonassisi, *MRS Commun.* **2015**, 5, 265.
- [33] J. Xu, J.-B. Liu, B.-X. Liu, B. Huang, *J. Phys. Chem. Lett.* **2017**, 8, 4391.
- [34] T. N. Huq, L. C. Lee, L. Eyre, W. Li, R. A. Jagt, C. Kim, S. Fearn, V. Pecunia, F. Deschler, J. L. MacManus-Driscoll, R. L. Z. Hoye, *Adv. Funct. Mater.* **2020**, 30, 1909983.
- [35] X. Zhang, M. E. Turiansky, C. G. Van de Walle, *J. Phys. Chem. C* **2020**, 124, 6022.
- [36] H. Jin, E. Debroye, M. Keshavarz, I. G. Scheblykin, M. B. J. Roeffaers, J. Hofkens, J. A. Steele, *Mater. Horiz.* **2020**, 7, 397.
- [37] R. H. Bube, *Photoelectronic Properties of Semiconductors*, Cambridge University Press, Cambridge, UK **1992**.
- [38] A. Rose, *Concepts in Photoconductivity and Allied Problems*, John Wiley & Sons, New York, NY **1963**.
- [39] A. Rose, *Phys. Rev.* **1955**, 97, 322.
- [40] N. Pai, J. Lu, T. R. Gengenbach, A. Seeber, A. S. R. Chesman, L. Jiang, D. C. Senevirathna, P. C. Andrews, U. Bach, Y. Cheng, A. N. Simonov, *Adv. Energy Mater.* **2018**, 9, 1803396.
- [41] R. L. Z. Hoye, R. E. Brandt, A. Oshero, V. Stevanovic, S. D. Stranks, M. W. B. Wilson, H. Kim, A. J. Akey, J. D. Perkins, R. C. Kurchin, J. R. Poindexter, E. N. Wang, M. G. Bawendi, V. Bulovic, T. Buonassisi, *Chem. – Eur. J.* **2016**, 22, 2605.
- [42] J. Pal, S. Manna, A. Mondal, S. Das, K. V. Adarsh, A. Nag, *Angew. Chem., Int. Ed.* **2017**, 56, 14187.
- [43] M. Abulikemu, S. Ould-Chikh, X. Miao, E. Alarousu, B. Murali, G. O. Ngongang Ndjawa, J. Barbé, A. El Labban, A. Amassian, S. Del Gobbo, *J. Mater. Chem. A* **2016**, 4, 12504.
- [44] F. Umar, J. Zhang, Z. Jin, I. Muhammad, X. Yang, H. Deng, K. Jahangeer, Q. Hu, H. Song, J. Tang, *Adv. Opt. Mater.* **2019**, 7, 1801368.
- [45] D. K. Schroder, in *Semiconductor Material and Device Characterization*, John Wiley & Sons, Inc., Hoboken, NJ, USA **2005**, pp. 251–317.
- [46] D. C. Look, in *Electrical Characterization of GaAs Materials and Devices*, John Wiley & Sons, Chichester **1989**, pp. 187–216.
- [47] A. Blondeel, P. Clauws, *J. Appl. Phys.* **1999**, 86, 940.
- [48] L. Xu, J. Wang, J. W. P. Hsu, *Phys. Rev. Appl.* **2016**, 6, 064020.
- [49] S. Wang, P. Kaienburg, B. Klingebiel, D. Schillings, T. Kirchartz, *J. Phys. Chem. C* **2018**, 122, 9795.
- [50] B. Saparov, F. Hong, J.-P. Sun, H.-S. Duan, W. Meng, S. Cameron, I. G. Hill, Y. Yan, D. B. Mitzi, *Chem. Mater.* **2015**, 27, 5622.
- [51] C. Lu, J. Zhang, H. Sun, D. Hou, X. Gan, M. H. Shang, Y. Li, Z. Hu, Y. Zhu, L. Han, *ACS Appl. Energy Mater.* **2018**, 1, 4485.
- [52] K. W. Jung, M. R. Sohn, H. M. Lee, I. S. Yang, S. Do Sung, J. Kim, E. Wei-Guang Diao, W. I. Lee, *Sustainable Energy Fuels* **2018**, 2, 294.
- [53] Y. Kim, Z. Yang, A. Jain, O. Voznyy, G.-H. Kim, M. Liu, L. N. Quan, F. P. García de Arquer, R. Comin, J. Z. Fan, E. H. Sargent, *Angew. Chem., Int. Ed.* **2016**, 55, 9586.
- [54] Z. Hu, Z. Wang, G. Kapil, T. Ma, S. Iikubo, T. Minemoto, K. Yoshino, T. Toyoda, Q. Shen, S. Hayase, *ChemSusChem* **2018**, 11, 2930.
- [55] B. Zhang, Y. Lei, R. Qi, H. Yu, X. Yang, T. Cai, Z. Zheng, *Sci. China Mater.* **2019**, 62, 519.
- [56] B.-B. Yu, M. Liao, J. Yang, W. Chen, Y. Zhu, X. Zhang, T. Duan, W. Yao, S.-H. Wei, Z. He, *J. Mater. Chem. A* **2019**, 7, 8818.
- [57] Z. Zhang, X. Li, X. Xia, Z. Wang, Z. Huang, B. Lei, Y. Gao, *J. Phys. Chem. Lett.* **2017**, 8, 4300.
- [58] X.-L. Li, L.-L. Gao, B. Ding, Q.-Q. Chu, Z. Li, G.-J. Yang, *J. Mater. Chem. A* **2019**, 7, 15722.
- [59] R. L. Z. Hoye, L. C. Lee, R. C. Kurchin, T. N. Huq, K. H. L. Zhang, M. Sponseller, L. Nienhaus, R. E. Brandt, J. Jean, J. A. Polizzotti, A. Kursumović, M. G. Bawendi, V. Bulović, V. Stevanović, T. Buonassisi, J. L. MacManus-Driscoll, *Adv. Mater.* **2017**, 29, 1702176.
- [60] Y. Peng, F. Li, Y. Wang, Y. Li, R. L. Z. Hoye, L. Feng, K. Xia, V. Pecunia, *Appl. Mater. Today* **2020**, 19, 100637.
- [61] P. C. Harikesh, H. K. Mulmudi, B. Ghosh, T. W. Goh, Y. T. Teng, K. Thirumal, M. Lockrey, K. Weber, T. M. Koh, S. Li, S. Mhaisalkar, N. Mathews, *Chem. Mater.* **2016**, 28, 7496.
- [62] F. Li, Y. Wang, K. Xia, R. L. Z. Hoye, V. Pecunia, *J. Mater. Chem. A* **2020**, 8, 4396.
- [63] P. Fan, H.-X. Peng, Z.-H. Zheng, Z.-H. Chen, S.-J. Tan, X.-Y. Chen, Y.-D. Luo, Z.-H. Su, J.-T. Luo, G.-X. Liang, *Nanomaterials* **2019**, 9, 1760.
- [64] M. Wang, P. Zeng, Z. Wang, M. Liu, *Adv. Sci.* **2020**, 7, 1903662.
- [65] D. Ju, X. Jiang, H. Xiao, X. Chen, X. Hu, X. Tao, *J. Mater. Chem. A* **2018**, 6, 20753.
- [66] R. A. Awni, Z. Song, C. Chen, C. Li, C. Wang, M. A. Razooqi, L. Chen, X. Wang, R. J. Ellingson, J. V. Li, Y. Yan, *Joule* **2020**, 4, 644.
- [67] O. Almora, M. García-Batlle, G. Garcia-Belmonte, *J. Phys. Chem. Lett.* **2019**, 10, 3661.
- [68] M. H. Futscher, M. K. Gangishetty, D. N. Congreve, B. Ehrler, *J. Chem. Phys.* **2020**, 152, 044202.
- [69] A. K. Jonscher, *J. Phys. D: Appl. Phys.* **1999**, 32, R57.
- [70] O. Almora, I. Zarazua, E. Mas-Marza, I. Mora-Sero, J. Bisquert, G. Garcia-Belmonte, *J. Phys. Chem. Lett.* **2015**, 6, 1645.
- [71] J. Xu, A. Buin, A. H. Ip, W. Li, O. Voznyy, R. Comin, M. Yuan, S. Jeon, Z. Ning, J. J. McDowell, P. Kanjanaboos, J.-P. Sun, X. Lan, L. N. Quan, D. H. Kim, I. G. Hill, P. Maksymovych, E. H. Sargent, *Nat. Commun.* **2015**, 6, 7081.
- [72] B. P. Nguyen, H. R. Jung, J. Kim, W. Jo, *Nanotechnology* **2019**, 30, 314005.
- [73] C. Hurtes, M. Boulou, A. Mitonneau, D. Bois, *Appl. Phys. Lett.* **1978**, 32, 821.
- [74] F. Biccari, N. Falsini, M. Bruzzi, F. Gabelloni, N. Calisi, A. Vinattieri, in *Defects in Functional Materials*, (Eds: F. C.-C. Ling, S. Zhou, A. Kuznetsov), World Scientific, Singapore **2020**, pp. 49–91.
- [75] L. K. Ono, S. (Frank) Liu, Y. Qi, *Angew. Chem., Int. Ed.* **2020**, 59, 6676.
- [76] A. Crovetto, A. Hajjafarassar, O. Hansen, B. Seger, I. Chorkendorff, P. C. K. Vesborg, *Chem. Mater.* **2020**, 32, 3385.

- [77] I. Turkevych, S. Kazaoui, E. Ito, T. Urano, K. Yamada, H. Tomiyasu, H. Yamagishi, M. Kondo, S. Aramaki, *ChemSusChem* **2017**, *10*, 3754.
- [78] H. C. Sansom, G. F. S. Whitehead, M. S. Dyer, M. Zanella, T. D. Manning, M. J. Pitcher, T. J. Whittles, V. R. Dhanak, J. Alaria, J. B. Claridge, M. J. Rosseinsky, *Chem. Mater.* **2017**, *29*, 1538.
- [79] Y. Yuan, V. Pecunia, in *2019 IEEE Int. Conf. Flex. Printable Sensors Syst.*, IEEE, Glasgow, UK **2019**, pp. 1–3.
- [80] L. Jiang, Y. Li, J. Peng, L. Cui, R. Li, Y. Xu, W. Li, Y. Li, X. Tian, Q. Lin, *J. Mater. Chem. C* **2020**, *8*, 2436.
- [81] Z. Li, G. Lakhwani, N. C. Greenham, C. R. McNeill, *J. Appl. Phys.* **2013**, *114*, 034502.
- [82] Z. Li, C. R. McNeill, *J. Appl. Phys.* **2011**, *109*, 074513.
- [83] F. Gao, Z. Li, J. Wang, A. Rao, I. A. Howard, A. Abrusci, S. Massip, C. R. McNeill, N. C. Greenham, *ACS Nano* **2014**, *8*, 3213.
- [84] M. Tapiero, N. Benjelloun, J. P. Zielinger, S. El Hamd, C. Noguét, *J. Appl. Phys.* **1988**, *64*, 4006.
- [85] D. V. Lang, *J. Appl. Phys.* **1974**, *45*, 3023.
- [86] A. M. Stoneham, *Theory of Defects in Solids*, Oxford University Press, Oxford, UK **2001**.
- [87] S. Heo, G. Seo, Y. Lee, D. Lee, M. Seol, J. Lee, J. B. Park, K. Kim, D. J. Yun, Y. S. Kim, J. K. Shin, T. K. Ahn, M. K. Nazeeruddin, *Energy Environ. Sci.* **2017**, *10*, 1128.
- [88] F. Brivio, K. T. Butler, A. Walsh, M. van Schilfgaarde, *Phys. Rev. B* **2014**, *89*, 155204.
- [89] L. M. Herz, *ACS Energy Lett.* **2017**, *2*, 1539.
- [90] Y. Fang, J. Huang, *Adv. Mater.* **2015**, *27*, 2804.
- [91] B. R. Sutherland, A. K. Johnston, A. H. Ip, J. Xu, V. Adinolfi, P. Kanjanaboos, E. H. Sargent, *ACS Photonics* **2015**, *2*, 1117.
- [92] G. Kresse, J. Furthmüller, *Phys. Rev. B* **1996**, *54*, 11169.
- [93] J. P. Perdew, K. Burke, M. Ernzerhof, *Phys. Rev. Lett.* **1996**, *77*, 3865.
- [94] P. E. Blöchl, *Phys. Rev. B* **1994**, *50*, 17953.
- [95] W. Kohn, L. J. Sham, *Phys. Rev.* **1965**, *140*, A1133.